ACS NANO

www.acsnano.org

ARTICLE

Self-Encapsulated 2D Electrenes: A Promising Platform for Various Emergent Properties

Shunuo Song, Zhenying Lin, Yan-Fang Zhang,* Lei Tao, Jingyu Yang, Yu-Yang Zhang,* and Shixuan Du

Cite This: *ACS Nano* 2025, 19, 39915−39924

Read Online

ACCESS | Metrics & More | Article Recommendations | Supporting Information

ABSTRACT: **Exploring unreported structural prototypes beyond conventional 2D electrides is crucial to overcome stability−functionality trade-offs and enable controlled interstitial anionic electron (IAEs) exposure. Given the correlation between 2D-distributed IAE configurations and structural topology, we identify MXene-like frameworks as ideal prototypes for electride design. By strategically substituting elements in the structural framework to construct electron-rich systems, we design a family of self-encapsulated electrides $M(M'X)_2$ featuring interlayer quasi-bonding, where both 0D- and 2D-distributed IAEs are confined within the structure. These materials, with the proposed synthesis through intercalation and high stability demonstrated after considering phase competition, enable controlled electron exposure owing to the low exfoliation energy and possess pseudoanionic electron sublattice dominant band characteristics near the Fermi level. $Mg(AlN)_2$ emerges as a topological 2D electrene. Ferromagnetic $Li(AlN)_2$ exhibits phase-dependent semiconducting/metallic characteristics. In addition, bilayer MgAlN obtained by either exfoliating the topmost AlN layer from $Mg(AlN)_2$ or depositing Mg onto the AlN monolayer demonstrates exceptional transition-metal-free ammonia synthesis activity, especially nitrogen activation activity due to the dual-origin nature of the IAEs, making it an intrinsic catalyst rather than a support. We report an electrene platform that allows for flexible encapsulation and exposure of IAEs. This platform serves as a highly active transition-metal-free catalyst in ammonia synthesis, suggesting promising opportunities for experimental exploration.**

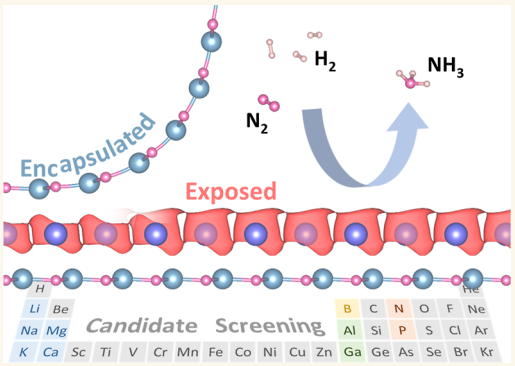

KEYWORDS: *self-encapsulated electrenes, transition-metal-free ammonia synthesis, theoretical design, topological electrenes, ferromagnetic electrenes*

1. INTRODUCTION

Electrides with monolayer thickness, referred to as electrenes,[1] are emerging two-dimensional (2D) materials where interstitial anionic electrons (IAEs) act as anions,[2] forming diverse IAE configurations ranging from 0D clusters to 2D planes. Examples include AlH_2[3] and Mo_2N[4] with 0D-distributed IAE character, Y_2Cl_3 and Sc_7Cl_{10}[5] presenting 1D-distributed IAE channels, and rare-earth chlorides (e.g., YCl[5]) or MXene-like materials (e.g., Ca_2N,[6,7] Y_2C,[8−10] Ca_2ZrN_2[11]) hosting intra-/interlayer 2D-distributed IAEs. The existence of 2D-distributed IAEs is typically linked to specific structural topologies, such as $R\bar{3}m$ (YCl,[5] Ca_2N[5,6]) or $P6_3/mmc$ ($BaCu$[12]), which explains why current electride design primarily relies on element substitution within known structural prototypes.[8,13,14] While this strategy has successfully generated MXene-like M_2X-type electrides, it neglects other MXene-like configurations with alternative stoichiometries or geometries. Moreover, electrides face stability−functionality trade-offs: IAEs in Y_2C and Sc_2C[14] are trapped within layers resulting in limited surface activity, while Ca_2N requires protective encapsulation to prevent electron loss.[15] Despite these challenges, the anionic electrons endow these materials with high electron density, low work functions,[4,16−18] and unique properties like superconductivity,[3,4,19] topological states,[10,20−24] and tunable magnetic properties,[24,25] making electrenes, especially electrenes with 2D-distributed IAEs (referred to as 2D electrenes), promising for applications in optoelectronic devices,[26−29] energy storage,[30] and catalysis.[30−42]

In particular, electrides have shown remarkable catalytic activity in various reactions,[2,33] such as hydrogenation reactions,[35] CO oxidation,[43] ammonia synthesis, and decomposition.[44] For instance, in ammonia synthesis, the rate-determining step (RDS), commonly regarded as N_2 dissoci-

Received: August 11, 2025
Revised: November 6, 2025
Accepted: November 7, 2025
Published: November 14, 2025

https://doi.org/10.1021/acsnano.5c13653
ACS Nano 2025, 19, 39915−39924

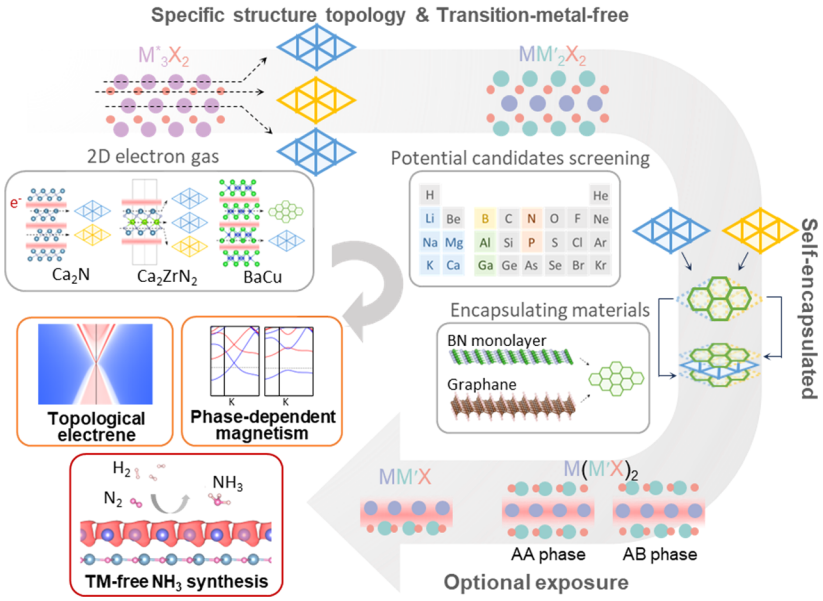

Figure 1. Design strategy for self-encapsulated 2D electrene $M(M'X)_2$ from a $M^*_3X_2$ prototype and potential properties and applications.

ation, is facilitated by the electron transfer from electrides to supported Ru nanoparticles (e.g., $Ru/Ca_{24}Al_{28}O_{64}$)[42] or to active sites in intermetallic electrides (e.g., LaRuSi).[36,38,45] These electrons weaken the N≡N bond, resulting in outstanding catalytic activity for NH_3 synthesis under mild reaction conditions. TMs are generally indispensable in most conventional ammonia synthesis systems, particularly for lowering the activation energy barrier of N_2 dissociation. Nevertheless, developing TM-free electride systems is crucial for sustainability,[46,47] since TM-based systems often rely on scarce and costly metals (e.g., Ru, Rh), limiting large-scale industrial deployment. TM-free alternatives could reduce such reliance and enable economically viable solutions. While current TM-free electride systems (e.g., Ba_2N [1.4 eV], Ca_2N [1.8 eV]) still exhibit higher N_2 activation barriers compared to TM-based counterparts (~1 eV), the pioneering studies have validated the feasibility of TM-free electrides functioning directly as ammonia synthesis catalysts, rather than merely as supports.[48] These findings motivate us to explore promising TM-free electrides that could rival or even surpass the catalytic performance of TM-based systems for ammonia synthesis.

In this work, guided by the symmetries of known electrides, $M^*_3X_2$, an MXene-like structure with $P\bar{3}m1$ symmetry, was selected as a potential prototype. Through element substitution, we predict a series of hitherto undiscovered self-encapsulated electrenes $M(M'X)_2$ (M = Li, Mg, or Ca; M′ = B, Al, or Ga; X = N, P). Potential candidates reveal that the IAEs in $M(M'X)_2$ are naturally confined as either 0D or 2D forms within the material. These materials have been proposed with high potential to be synthesized through intercalation and high stability retained following phase competition. Critically, one of the outermost MX layers can be exfoliated to form a stable MM′X, exposing the IAEs on one side while maintaining its encapsulation on the other side, facilitating potential applications. Interestingly, $Mg(AlN)_2$ in AB phase exhibits topologically nontrivial features, while $Li(AlN)_2$ hosts spin-polarized IAEs. Specifically, $Li(AlN)_2$ in the AA phase is a semiconductor exhibiting 0D-distributed IAEs, and the AB phase is a metal with a 2D-distributed IAE character. For catalytic applications, MgAlN achieves a zero-energy barrier between the chemically adsorbed state and the final fully dissociated state in a TM-free system, surpassing the N_2 activation capabilities of previously reported electrides, including both TM-free and TM-containing systems. Moreover, the subsequent ammonia formation process exhibits a maximum energy barrier of 1.52 eV, comparable to those observed in existing systems, advancing in TM-free ammonia synthesis catalysts.[30,40]

2. RESULTS AND DISCUSSION

2.1. Design and Screening of Self-Encapsulated MXene-Like Electrenes with Various Emergent Properties.

2.1.1. Design Rule. $P\bar{3}m1$ symmetry was selected as the design foundation because it represents the monolayer symmetry of the Ca_2N-like family of 2D electrenes, which is one of the most numerous classes of established 2D electrenes. Inspired by MXenes for their compositional diversity within shared $P\bar{3}m1$ symmetry, we propose a symmetry-driven design strategy for electrenes through replacing TMs in an MXene prototype configuration ($M^*_3X_2$) to screen and develop the $M(M'X)_2$ family. This approach ensures the materials maintain MXene-like atomic layer configurations while exploring variations in symmetry phases (e.g., $P\bar{6}m2$ for the AA phase and $P\bar{3}m1$ for the AB phase) to optimize the electrene behavior. As shown in Figure 1, MM'_2X_2 exhibits a five-atomic-layer structure, where M and M′ represent the metal elements in the middle layer and those in the outermost layer, respectively. The selection of element substitution requires the following three key considerations. First, while MXene-based electrides with TM atoms have been widely explored,[4,49] main-group metal elements remain relatively unexplored. Thus, it is intriguing to focus on TM-free electrides that can complement traditional TM-based electrides. In addition, TM-free systems are easier to simulate first-principles calculations, avoiding the strong electron correlations and complex oxidation states of transition metals and facilitating efficient material screening and mechanism understanding. Second, unlike the reported electron-neutral and electron-deficient electrides that need external modulations (e.g., strain or

https://doi.org/10.1021/acsnano.5c13653
ACS Nano 2025, 19, 39915−39924

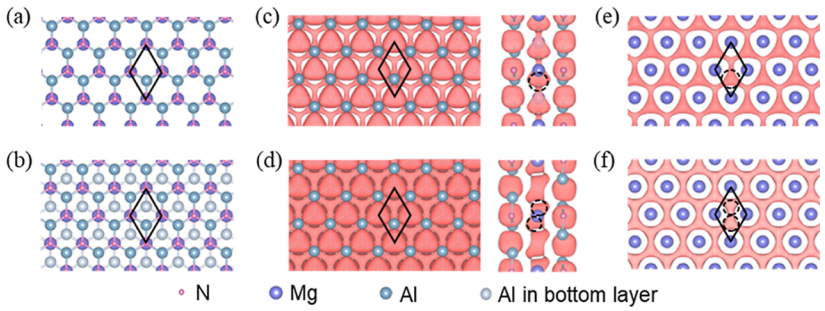

Figure 2. Representative atomic structures and the corresponding spatial distribution of IAEs in the 2D electrene $M(M'X)_2$, exemplified by AA- and AB-phase $M(M'X)_2$. (a,b) Top views of $Mg(AlN)_2$ in AA and AB phases. (c,d) Top and side views of the electron localization function (ELF) map for AA- and AB-phase $Mg(AlN)_2$ with an isosurface value of 0.6, respectively. (e,f) Slab cuts on the Mg layer of the ELF map for AA- and AB-phase $Mg(AlN)_2$, with dashed circles highlighting the regions where electrons are well-localized.

pressure) to provide IAEs in interstitial spaces,[16,50] we prioritize materials with intrinsic electron-rich characteristics. Such characteristics arise from imbalances between cation and anion charges, which facilitate the generation of IAEs at interstitial sites and thus simplify the preparatory steps for their potential practical application. Lastly, elements from the first and second main groups of the periodic table with low electronegativity (<1.5, Pauling scale) are selected as potential donors of IAEs, thereby contributing to the formation of stable encapsulated electron-rich regions essential for the electrene behavior in the middle of a sandwiched structure.

Following the above design rule, s-block metal elements are used to replace the middle M* layer in $M^*_3X_2$. The top/bottom M* and X are selected from electron-neutral IIIA−VA insulators (e.g., Al−N), both of which meet the needs of symmetry and encapsulation. The operation ensures both electron-rich characteristics and structural compatibility, introducing a pathway for exploring electrenes with tailored electronic properties.

2.1.2. Structure of $M(M'X)_2$. In the relaxed configurations, the middle M layer is sandwiched between h-BN-like M′X layers, with M′ atoms buckled inward. Based on the stacking mode of the top and bottom M′X layers, the phase with completely aligned orientations is termed "AA", while that with inconsistent orientations is termed "AB". Figure 2a,b illustrates the top view of the AA and AB phases, showing that both phases of $M(M'X)_2$ adopt a hexagonal structure. The AA and AB phases belong to the $P\bar{6}m2$ and $P\bar{3}m1$ space groups, respectively. The optimized lattice parameters are listed in Table S1 and in the Supporting Information. The in-plane lattice parameters of $M(M'X)_2$ deviate by less than 5% from those of the corresponding parent bulk III−V compounds. The small deviation implies that substituting s-block metals induces minor structural changes, suggesting that intercalation is a feasible approach to achieve $M(M'X)_2$ (discussed in the Supporting Information). In addition, the small lattice variation indicates that the interstitial space available for IAE formation decreases as the atomic radius of the s-block metal increases, implying a reduction in the dimensionality of the IAE distribution.

2.1.3. Distribution of IAEs in $M(M'X)_2$. After a high-throughput screening, we identified a total of 11 types of stable electrenes (4 of them are 2D electrenes) from 60 candidates through evaluating ELF and projected density of states (PDOSs).[51−53] All of these electrenes exhibit localized electrons at the interstitial space with an isosurface value of ELF over 0.5. In addition, the PDOS is used to verify that the electronic states near the Fermi level mainly contribute from the localized electrons at the interstitial space.

Figure 2d−f presents the ELF maps with an isosurface value of 0.6 for $Mg(AlN)_2$ in AA and AB phases, exemplifying the distribution of IAEs in 2D $M(M'X)_2$ electrenes (Figure 2c,d shows both the top and side views, while Figure 2e,f provides the distribution of IAEs in the Mg layer.). The black solid diamond in the figures represents the primitive cell used for calculations. The black dashed circle highlights the high-electron-density region within the interconnected 2D-distributed IAEs, located inside the tetrahedron formed by three adjacent Mg atoms and the nearest Al atom. Similarly, the electron-rich region is also located at this position in the screened-out 0D $M(M'X)_2$ electrenes (Figure S3). The diversity of dimensionality of the IAEs confirms the former analysis of their atomic-radius-dependent behavior due to the small intercalation-induced lattice change. As the atomic radius of s-block metals increases, the anionic electrons become confined within 0D cages rather than in 2D planes, thereby limiting the formation of 2D electrenes.

2.1.4. Stability and Synthesis Proposal of $M(M'X)_2$. Thermodynamic stability was systematically evaluated through phonon dispersion spectra, ab initio molecular dynamics simulations, cohesive energy (with reference to single-atom energy), and formation energy analysis relative to elemental precursors. All of the calculated phonon dispersion spectra of the identified 11 $M(M'X)_2$ compounds show no imaginary frequencies (Figure S4), confirming their intrinsic stability. Additionally, room-temperature ab initio molecular dynamics simulations of the 11 screened electrenes further support the dynamic stability, with negligible structural deviations observed over extended simulation times (10 ps in Figure S5). All 11 electrenes exhibit negative cohesive and formation energies (Table S1), indicating that these materials are energetically favorable and can be synthesized under appropriate conditions. While these analyses, including the intact structure at room temperature, suggest the potential stability of the materials, they provide necessary rather than sufficient conditions for stability. Computational methods, though insightful, have limitations due to the idealized nature of theoretical models compared to real experimental conditions. To bridge this gap, we propose the following potential experimental synthesis routes, offering practical guidance for their realization in the laboratory.

Although $M(M'X)_2$ cannot be prepared using conventional MXene synthesis methods such as etching, recent advances on atomic intercalation techniques show promise.[54−56] Taking

https://doi.org/10.1021/acsnano.5c13653
ACS Nano 2025, 19, 39915−39924

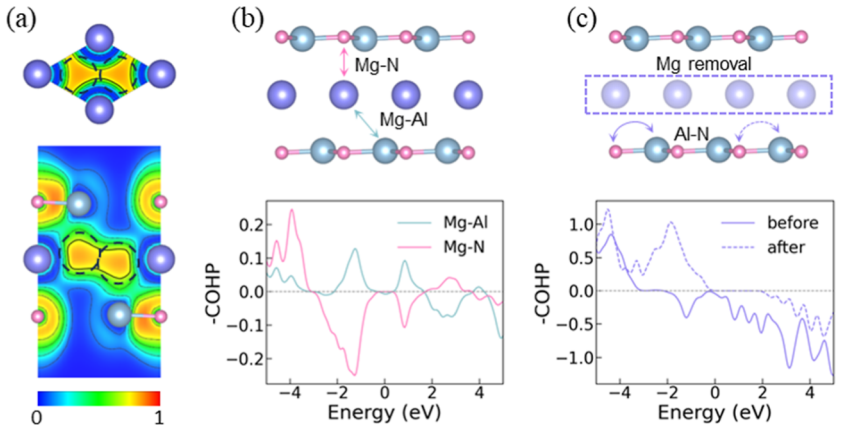

Figure 3. IAEs in the Mg layer and interlayer quasi-bonds between the AlN layer and Mg layer in the 2D electrene $Mg(AlN)_2$ of AB phase. (a) Slab cuts of the ELF maps on the Mg layer (upper panel) and along the [110] direction (lower panel) of the $Mg(AlN)_2$ primitive cell. Dashed circles denote the site of empty spheres with a Wigner−Seitz radius of 1.0 Å. (b) −COHP curves of Mg−N and Mg−Al in $Mg(AlN)_2$. (c) −COHP curves of Al−N before and after Mg removal in $Mg(AlN)_2$.

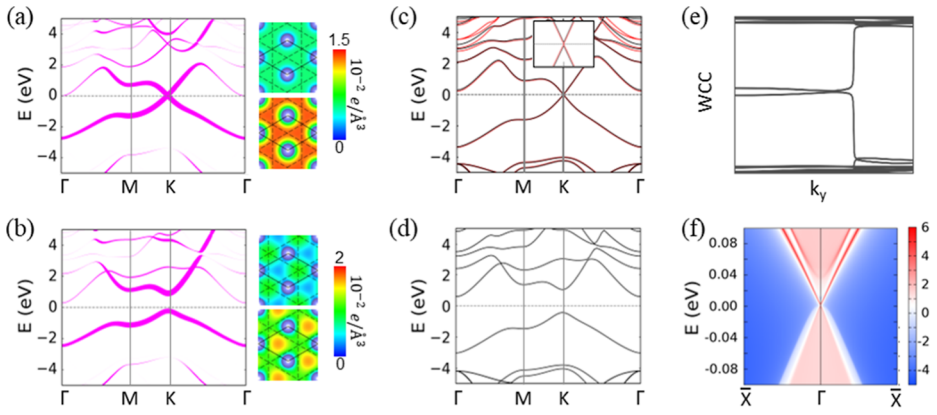

Figure 4. Electronic properties of 2D electrene $Mg(AlN)_2$ in AB and AA phases. (a,b) Projected PBE band structures on the empty spheres (left panel) and slab cuts of the partial charge density maps on the Mg layer corresponding to the highest valence band (lower right panel) and lowest conduction band (upper right panel) of $Mg(AlN)_2$ in AB and AA phases, respectively. (c,d) HSE band structures of $Mg(AlN)_2$ in AB and AA phases. The red lines in (c) represent the band structures with SOC, and the inset shows a zoomed-in view around the Fermi level in AB-phase $Mg(AlN)_2$. (e) Evolution lines of Wannier centers for AB-phase $Mg(AlN)_2$ in the k_z = 0 plane. (f) Nontrivial topological edge states in AB-phase $Mg(AlN)_2$.

$Mg(AlN)_2$ as an example, the two target phases shown in Figure 2 have the lowest formation energies among all possible phases derived from Mg intercalation into AA- and AB-stacked AlN bilayers. It highlights the energetic feasibility of synthesizing these phases through intercalation. Detailed information can be found in the phase competition discussions of $Mg(AlN)_2$ synthesis through intercalation (Figure S6). Furthermore, $M(M'X)_2$ shows the potential to form multilayer structures through specific interlayer bonding modes (Figure S7), thus providing flexibility for device applications.

In addition, air stability is a key challenge for electrene applications in preventing IAEs exhaust through the adsorption of molecules such as oxygen and water on the surface. In the case of $M(M'X)_2$, the outermost X atoms are IIIA elements rather than metal elements, similar to YCl-type electrenes where halogens remain in the outermost layer. The presence of IIIA elements in the outermost layer hinders the chemical adsorption of oxygen and water molecules. These molecules tend to interact physically with the surface, maintaining a molecule−surface distance over 3 Å. The physical adsorption effectively prevents charge transfer and preserves the IAEs, demonstrating the self-encapsulation capability of the $M(M'X)_2$ system.

2.2. Origin of IAEs and Intralayer Quasi-Bonds. The origin of IAEs can be understood via electron localization and bonding analysis. In Figure 3a, the ELF contour plot illustrates highly localized electrons in $Mg(AlN)_2$ (AB phase), with the bold 0.7 contour line highlighting the connectivity of the 2D-distributed IAEs. The IAEs exist not only in the interstitial voids inherent to the Mg atomic layer but also close to the Al atoms in the AlN layer, indicating a dual-origin nature of the IAEs. One component corresponds to Mg-layer vacancies dominated by Mg electrons, while the other floats on the inward-buckled surface of the Al atoms, like dangling bond electrons.

A freestanding Mg monolayer without the outermost AlN layers presents similar 2D-distributed IAEs localized in the interstitial voids (Figure S8a). However, the freestanding Mg monolayer is dynamically unstable (soft phonon modes in Figure S8b). The 2D-distributed IAEs in $Mg(AlN)_2$ are stabilized through interlayer interactions, explained as follows. The crystal-orbital Hamiltonian population analysis (Figure 3b) shows no bonding between Mg and N (-ICOHP <0.1),

https://doi.org/10.1021/acsnano.5c13653
ACS Nano 2025, 19, 39915−39924

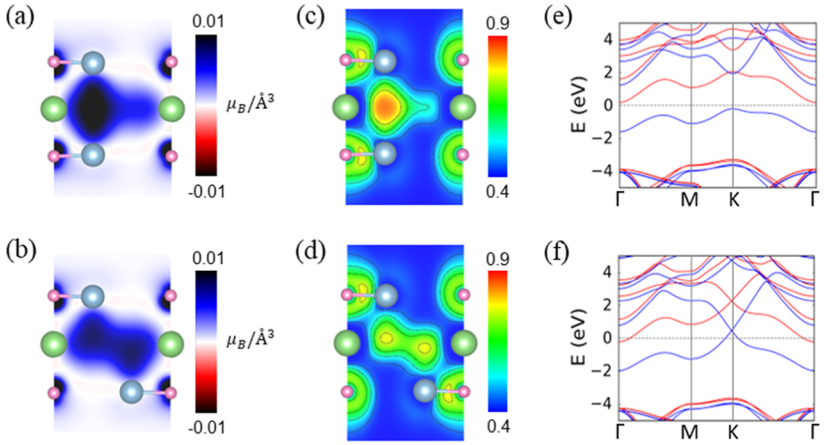

Figure 5. Electronic properties of 0D magnetic electride AA-phase $Li(AlN)_2$ and 2D magnetic electride AB-phase $Li(AlN)_2$. (a,b) Slab cuts of the magnetization density maps along the [110] direction of the AA- and AB-phase $Li(AlN)_2$ primitive cells, respectively. (c,d) Slab cuts of the ELF maps along the [110] direction of the AA- and AB-phase $Li(AlN)_2$ primitive cells, respectively. (e,f) HSE band structures of $Li(AlN)_2$ in AA and AB phases. The blue and red lines represent the spin-up and spin-down channels, respectively.

while Mg−Al bonding states dominate below the Fermi level. Further analysis of the −COHP curves between Al and N before and after Mg removal (Figure 3c) shows that removing Mg shifts Al−N antibonding states above the Fermi level, strengthening the Al−N bond. In Mg-free AlN, Al−N bonding states are fully occupied, while antibonding states are empty. In $Mg(AlN)_2$, Al−N antibonding states are present below the Fermi level, suggesting that the presence of Mg layer reduces Al−N interaction. The bonding analysis indicates that Mg interacts with Al, enabling Mg layers to stably exist between AlN layers.

The role of the interlayer interaction is further explored by comparing the AB-phase $Mg(AlN)_2$ with the dynamically unstable AB-phase $Mg(BN)_2$. The difference originates from their nitride-layer characteristics inherited from bulk behaviors. Bulk BN naturally features strong in-plane B−N π bonding with weak interlayer forces, while bulk AlN forms a 3D diamond-like network through sp^3 hybridization. The planar π bonding in the BN layer remains upon Mg intercalation, inhibiting effective Mg bonding with the occupied Mg−B/N antibonding states (Figure S9). In contrast, the relative weaker Al−N π interactions allow bond reorganization during Mg intercalation, which enables quasi-bond interactions. The quasi-bond nature of interlayer interaction in $Mg(AlN)_2$ is supported by a cleavage energy of 1.06 J/m^2 (Figure S10) and an interlayer distance of 2.53 Å (typical van der Waals gaps >3.0 Å). The phonon spectrum, which shows no imaginary frequencies, indicates that MgAlN remains dynamically stable after the exfoliation of one of the outermost AlN layers. It is worth noting that the 2D-distributed IAEs are exposed at the surface in the Mg layer with an unchanged low work function of 3.09 eV, making it flexible to be encapsulated or exposed.

2.3. Phase-Controlled Electronic and Topological Band Engineering in 2D $M(M'X)_2$. By comparing the band structures of AB-phase $Mg(AlN)_2$ with those of the AlN bilayer and Mg monolayer (Figure S11), it is evident that the bands of the Mg monolayer appear within the band gap of AlN, giving the $Mg(AlN)_2$ system a metallic character. The band structure (left panels of Figure 4a,b) and DOS (Figure S12) projected onto the empty spheres further confirm the contribution of the IAEs to the bands near the Fermi level. Considering the IAEs as pseudoanions, the 2D-distributed IAEs in AB-phase $Mg(AlN)_2$ can be viewed as a slightly buckled hexagonal sublattice, verified by the partial charge density map shown in the right panels in Figure 4a.[57] The bands show 4-fold degeneracy at the high-symmetry *K*-point, even at the HSE level (Figure 4c). All $M(M'X)_2$ compounds in AB phase share the same buckled hexagonal lattice for their pseudoanionic IAEs, leading to the consistent presence of 4-fold degeneracy (2-fold degeneracy in each spin channel for magnetic systems) at the high-symmetry *K*-point, with slight energy shifts (Figure S13).

However, the 4-fold degeneracy band characteristic vanishes in the AA phase. For example, the vertically aligned Al atoms in $Mg(AlN)_2$ (AA phase) induces a different structure topology of the pseudoanionic IAEs (right panels of Figure 4b). The symmetry change degenerates the excess electron-dominated bands at the *K*-point, resulting in the absence of the crossing at the *K*-point (Figure 4b,d). Consequently, $M(M'X)_2$ electrenes exhibit different electronic structures in AA and AB phases, such as the transition from metallic (AB-phase $Li(AlN)_2$) to semiconducting states (AA-phase $Li(AlN)_2$).

The hexagonal lattice of the pseudoanionic IAEs in $M(M'X)_2$ (AB phase) and the Dirac point at *K*-point suggest a possible topological material behavior.[58] Taking the AB-phase $Mg(AlN)_2$ as an example, the Dirac point degenerates when SOC is considered (Figure 4c, HSE level), opening a 15 meV band gap. The odd-numbered intersections between the reference lines and Wannier center trajectories in the $k_z = 0$ plane (Figure 4e) provide direct evidence that the AB-phase $Mg(AlN)_2$ is a 2D topological insulator. According to the bulk-boundary correspondence principle, within the SOC-induced gap, nontrivial one-dimensional edge states connecting the conduction band and valence band, protected by time-reversal symmetry, can be observed, as shown in Figure 4f.

2.4. Ferromagnetic 2D Electrene $Li(AlN)_2$. Among all the potential $M(M'X)_2$ electrenes, $Li(AlN)_2$ and $Ca(BP)_2$ in both phases, $Ca(AlN)_2$ in the AA phase, and $Ca(AlP)_2$ and $Ca(GaP)_2$ in the AB phase exhibit magnetic properties. Nonmagnetic (NM) and three magnetic states, including ferromagnetic (FM), zigzag antiferromagnetic (AFM1), and collinear antiferromagnetic (AFM2), were explored (Figure S14). Taking $Li(AlN)_2$ as an example, the magnetic moments and the relative energies of various magnetic states relative to

https://doi.org/10.1021/acsnano.5c13653
ACS Nano 2025, 19, 39915−39924

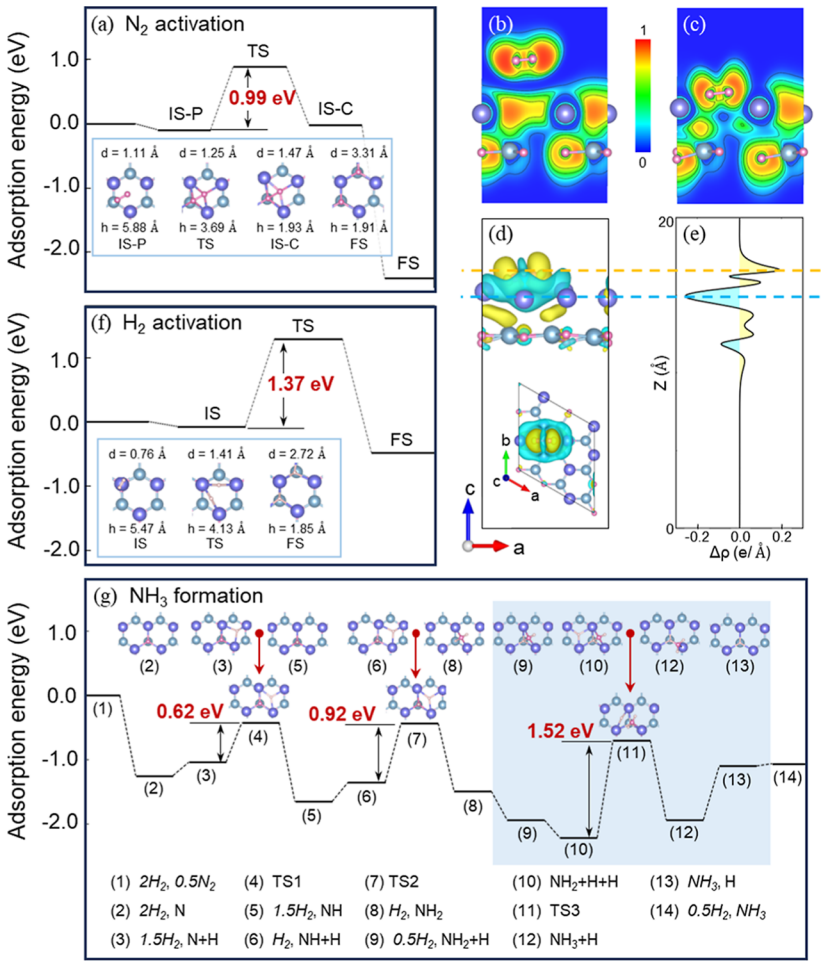

Figure 6. Ammonia synthesis on MgAlN. (a) Energy profile for N_2 activation on MgAlN, where d represents the bond length of N−N, and h denotes the vertical distance between the left-side N and the nearest neighboring Al. (b, c) Slab cuts of the ELF maps along the [1$\bar{2}$0] direction of the supercell in the IS-P and TS states in the N_2 activation process, respectively. (d) Side view of the charge density difference of N_2 absorbed on MgAlN in the TS state (with the top view shown in the inset) and (e) corresponding planar averaged charge density difference. Electron accumulation and depletion are represented by yellow and cyan, respectively. (f) Energy profile for H_2 activation on MgAlN, where d represents the bond length of H−H and h denotes the vertical distance between the left-side H and the nearest neighboring Al. (g) Energy profiles for NH_3 formation on MgAlN. The unabsorbed gas-phase molecules are represented with italicized text. In the light-blue-marked region, the active sites are saturated with H. The "NH_3, H" step to the final state "$0.5H_2$, NH_3" is included for energy reference.

the magnetic ground states are listed in Table S2, showing that both the AA- and AB-phase $Li(AlN)_2$ exhibit ferromagnetic ground states, with a magnetic moment of 0.97 and 0.90 μ_B per formula unit, respectively, which is roughly equivalent to the number of IAEs in the system.

Figure 5a,b shows the spin charge density maps for the AA and AB phases, where the distribution of magnetic charge closely matches the distribution of IAEs in the ELF maps of the AA and AB phases shown in Figure 5c,d. The agreement indicates that the magnetism is primarily contributed by the IAEs in the interstitial spaces, a phenomenon commonly termed interstitial magnetism (IM). Although no magnetic atoms are present, the unique characteristics of the IAEs and their interactions lead to the emergence of ferromagnetic states in both phases. While the DFT results establish the ferromagnetic ground state and provide a baseline understanding of the magnetic interactions, it is worth noting that the nonlocal direct exchange interactions (atomic orbital-free magnetism) among these IAEs may not be fully captured. Future investigations are needed by employing advanced methods such as constrained random phase approximation, which has been successfully applied in the case of 0D electrene (named as 2D electrides in the reference) like $LaBr_2$.[59] Such methods would be particularly valuable in elucidating the long-range exchange interactions and their contribution to the magnetic stability of these materials.

From the morphology of the IAEs in Figure 5c,d, it is evident that $Li(AlN)_2$ in the AA phase is a 0D electrene with a triangular distribution of the IAEs, while $Li(AlN)_2$ in the AB phase is a 2D electrene with a hexagonal distribution of the IAEs. Combining the HSE band structures (Figure 5e,f), both the AA and AB phases show ferromagnetic properties. However, the AA-phase $Li(AlN)_2$ is a semiconductor, while the AB-phase is a metal. The rich differences in the electronic and magnetic properties between the two phases of the $M(M'X)_2$ system suggest $M(M'X)_2$ as a potential platform for tailoring the material properties.

2.5. MgAlN in Ammonia Synthesis. As discussed earlier, the quasi-bond nature of interlayer interactions in $M(M'X)_2$ electrenes enables the encapsulated IAEs to be exposed unilaterally through exfoliation of one outermost M′X layer. Notably, the MM′X bilayer exhibits similar dual-origin IAE

https://doi.org/10.1021/acsnano.5c13653
ACS Nano 2025, 19, 39915−39924

characteristics compared to that before exfoliation, making it an ideal candidate for ammonia synthesis as an intrinsic catalyst rather than a catalyst support, as demonstrated below with MgAlN as an example. Additionally, depositing M atoms on an M′X monolayer has been proposed as an alternative synthesizing approach to obtain MM′X electrenes (see Section 8 in Supporting Information). Thus, the potential application of MgAlN in ammonia synthesis is investigated as follows.

The adsorption energies of N_2 on the MgAlN surface are −94 and −25 meV for physical and chemical adsorption, respectively, while a barrier of 0.99 eV occurs for the physical adsorbed state (IS−P) transiting to the chemical adsorbed state (IS−C), as shown in Figure 6a. The ELF map of the IS-P state (Figure 6b) shows the localized IAEs in the interstitial voids close to the N_2 adsorption site. In contrast, the transition state (TS, Figure 6c) demonstrates the disappearance of the localized IAEs and the transfer of electrons from the interstitial voids to the N_2 molecule. The charge density difference plot and the planar averaged charge density difference of N_2/MgAlN (Figure 6d,e) further reveal that the electrons transfer to the N_2 molecule from structural voids rather than atomic sites.

In the IS-C state, one N atom resides at the active site (the hollow site of the surface Mg atoms with an Al atom located directly below), while the other N atom is positioned between a bridge site and a hollow site without an underlying atom. In this configuration, the N−N bond length is stretched by 0.35 Å compared to the gas-phase and IS-P states. This indicates a N_2 preactivation which accounts for the relatively low adsorption energy. The preactivated N_2 can simultaneously transit to a fully dissociated state (FS), with an N−N distance of 3.31 Å, without any energy barrier. It demonstrates the excellent catalytic performance of MgAlN in N_2 activation. Notably, the temperature dependence of gas molecules exerts a more pronounced influence on this initial adsorption process compared to the subsequent complete dissociation process.

H_2 is found physically adsorbed on the MgAlN surface with an adsorption energy of −63 meV. As shown in Figure 6f, the hydrogen dissociation process involves two key steps: (1) initial adsorption of H_2 at the Mg top site and (2) complete dissociation into two H atoms with an H−H distance of 2.72 Å. The process requires overcoming an energy barrier of 1.37 eV, which is slightly higher than the barrier for N_2 activation. The higher barrier for H_2 dissociation effectively suppresses hydrogen poisoning by limiting excessive H atom adsorption.

The catalytic performance is further evaluated by analyzing the energy barriers involved in the NH_3 synthesis process (as shown in Figure 6g). The energy barriers for the formation of NH, NH_2 intermediates, and the product NH_3 on MgAlN are 0.62 0.93, and 1.52 eV, respectively. This indicates that the RDS in NH_3 synthesis on MgAlN has an energy barrier of 1.52 eV, which is comparable to that in previously reported systems such as Y_5Si_3 (1.65 eV) and Ru/LaCoSi (1.45 eV). In the insets in Figure 6g, it can be observed that during the reaction, the N atom and the NH intermediates both occupy the active site, while the NH_2 complex moves away from the active site and occupies a bridge site. When the active site is free, H atoms preferentially occupy it. However, once the active site is saturated with H, subsequent H atoms will bond with the NH_2 complex to form the final product, NH_3. Meanwhile, the energy barrier for H diffusion between two active sites on the MgAlN surface is only 0.38 eV, allowing the H-saturated reaction sites to be easily regenerated and to continuously catalyze the reaction.

3. CONCLUSION

In conclusion, leveraging the relationship between 2D-distributed IAEs configurations and structural topology, we proposed MXene-like structures as versatile prototypes for 2D electride design. Starting from the five-atomic-layer $M^*_3X_2$ prototype, we have successfully screened out a family of self-encapsulated electrenes $M(M'X)_2$ with high stability and promising ease of fabrication, comprising 11 0D and 4 2D electrenes. It has been demonstrated that the IAEs in $M(M'X)_2$ can be controllably exposed through the exfoliation of one M'X layer, facilitated by the interlayer quasi-bonding interactions. Notably, the electronic bands near the Fermi level are mainly contributed by IAEs and exhibit pseudoanionic electron sublattice-governed band characteristics. $Mg(AlN)_2$ in AB phase emerges as a topological 2D electrene, while $Li(AlN)_2$ in AA and AB phases are both ferromagnetic, with the former showing semiconducting and the latter exhibiting metallic properties. In addition, bilayer MgAlN exhibits excellent catalytic activity in ammonia synthesis, suggesting the potential of TM-free electrides to function as independent ammonia synthesis catalysts, which expands their traditional applications as catalyst supports. These findings not only validate the potential of MXene-like structures as electride hosts but also expand the research scope of electrenes.

4. METHODS

First-principles calculations were performed using the Vienna Ab initio Simulation Package (VASP).[60,61] Core−valence interactions were described by the projector-augmented wave method.[62] The Perdew−Burke−Ernzerhof (PBE) exchange−correlation functional within generalized gradient approximation was adopted.[63] Furthermore, hybrid Heyd−Scuseria−Ernzerhof (HSE06) functional was also employed to get more accurate band structures.[64] A vacuum space larger than 15 Å was employed to eliminate the artificial interactions between periodic images. In our calculation, the kinetic energy cutoff of the plane-wave basis is 520 eV. A 12 × 12 × 1 Γ-centered Monkhorst−Pack k-sampling mesh[65] was used for the primitive cell, 6 × 5 × 1 *k*-mesh for the magnetic unit cell, and 3 × 3 × 1 *k*-mesh for the ammonia synthesis supercell. The DFT-D3 method of Grimme was incorporated to account for van der Waals interactions.[66] Dipole correction was applied for all of the asymmetric slab calculations. Structural optimizations were performed until atomic forces converged below 0.001 eV/Å and total energy differences were less than 10^{-8} eV. Ab initio molecular dynamics simulations (AIMD) were performed under an *NVT* ensemble with a temperature of 300 and 923 K using 4 × 4 × 1 supercells for $M(M'X)_2$ and 7 × 7 × 1 supercells for MgAlN, respectively. Phonon dispersion spectra were obtained using the finite-displacement method, as implemented in the Phonopy code.[67] The edge states and Wannier charge centers were calculated by using a tight-binding Hamiltonian constructed on the basis of maximally localized Wannier functions implemented in Wannier90 and WannierTools codes.[68−70] The energy barrier for the elementary steps of ammonia synthesis was calculated using the climbing image-nudged elastic band by VASP and VTST packages.[71−74]

ASSOCIATED CONTENT

Supporting Information

The Supporting Information is available free of charge at https://pubs.acs.org/doi/10.1021/acsnano.5c13653.

Optimized lattice constants, cohesive energies, formation energies, magnetic properties, work functions, ELF

https://doi.org/10.1021/acsnano.5c13653
ACS Nano 2025, 19, 39915−39924

maps, phonon dispersions, AIMD simulations, electronic band structures and PDOS, cleavage energy of identified electrenes; ammonia synthesis, and hydrogen diffusion (PDF)

AUTHOR INFORMATION

Corresponding Authors

Yan-Fang Zhang − *University of Chinese Academy of Sciences and Beijing National Laboratory for Condensed Matter Physics and, Institute of Physics, Chinese Academy of Sciences, Beijing 100190, P. R. China*; Email: zhangyuyang@ucas.ac.cn

Yu-Yang Zhang − *University of Chinese Academy of Sciences and Beijing National Laboratory for Condensed Matter Physics and, Institute of Physics, Chinese Academy of Sciences, Beijing 100190, P. R. China*; orcid.org/0000-0002-9548-0021; Email: zhangyanfang@ucas.ac.cn

Authors

Shunuo Song − *University of Chinese Academy of Sciences and Beijing National Laboratory for Condensed Matter Physics and, Institute of Physics, Chinese Academy of Sciences, Beijing 100190, P. R. China*

Zhenying Lin − *University of Chinese Academy of Sciences and Beijing National Laboratory for Condensed Matter Physics and, Institute of Physics, Chinese Academy of Sciences, Beijing 100190, P. R. China*; Present Address: Beijing JWGB Instrument Co., Ltd., Beijing 100176, P. R. China

Lei Tao − *University of Chinese Academy of Sciences and Beijing National Laboratory for Condensed Matter Physics and, Institute of Physics, Chinese Academy of Sciences, Beijing 100190, P. R. China*

Jingyu Yang − *University of Chinese Academy of Sciences and Beijing National Laboratory for Condensed Matter Physics and, Institute of Physics, Chinese Academy of Sciences, Beijing 100190, P. R. China*; orcid.org/0000-0003-2299-3966

Shixuan Du − *University of Chinese Academy of Sciences and Beijing National Laboratory for Condensed Matter Physics and, Institute of Physics, Chinese Academy of Sciences, Beijing 100190, P. R. China; Songshan Lake Materials Laboratory, Dongguan 523808, P. R. China*; orcid.org/0000-0001-9323-1307

Complete contact information is available at: https://pubs.acs.org/10.1021/acsnano.5c13653

Notes

The authors declare no competing financial interest.

ACKNOWLEDGMENTS

This work was supported by the National Key R&D program of China (Grant No. 2024YFA1207800), the National Natural Science Foundation of China (Grants No. 92477205 and No. 52250402), CAS Project for Young Scientists in Basic Research (YSBR-003), and the Fundamental Research Funds for the Central Universities.

REFERENCES

(1) Druffel, D. L.; Woomer, A. H.; Kuntz, K. L.; et al. Electrons on the surface of 2D materials: from layered electrides to 2D electrenes. *J. Mater. Chem. C* **2017**, *5* (43), 11196−11213.

(2) Hosono, H.; Kitano, M. Advances in Materials and Applications of Inorganic Electrides. *Chem. Rev.* **2021**, *121* (5), 3121−3185.

(3) Yang, Q. P.; Jiang, X.; Zhao, J. J. Coexistence of Zero-Dimensional Electride State and Superconductivity in AlH_2 Monolayer. *Chin. Phys. Lett.* **2023**, *40* (10), 107401.

(4) Pereira, Z. S.; Faccin, G. M.; da Silva, E. Z. Strain-induced multigap superconductivity in electrene Mo_2N: a first principles study. *Nanoscale* **2022**, *14* (24), 8594−8600.

(5) Wan, B.; Lu, Y. F.; Xiao, Z. W.; Muraba, Y.; Kim, J.; Huang, D.; Wu, L.; Gou, H.; Zhang, J.; Gao, F.; et al. Identifying quasi-2D and 1D electrides in yttrium and scandium chlorides via geometrical identification. *npj Comp. Mater.* **2018**, *4* (1), 77−79.

(6) Lee, K.; Kim, S. W.; Toda, Y.; et al. Dicalcium nitride as a two-dimensional electride with an anionic electron layer. *Nat.* **2013**, *494* (7437), 336−340.

(7) Druffel, D. L.; Kuntz, K. L.; Woomer, A. H.; et al. Experimental Demonstration of an Electride as a 2D Material. *J. Am. Chem. Soc.* **2016**, *138* (49), 16089−16094.

(8) Tada, T.; Takemoto, S.; Matsuishi, S.; et al. High-throughput ab initio screening for two-dimensional electride materials. *Inorg. Chem.* **2014**, *53* (19), 10347−10358.

(9) Inoshita, T.; Hamada, N.; Hosono, H. Ferromagnetic instability of interlayer floating electrons in the quasi-two-dimensional electride Y_2C. *Phys. Rev. B* **2015**, *92* (20), 201109.

(10) Huang, H.; Jin, K. H.; Zhang, S.; et al. Topological Electride Y_2C. *Nano Lett.* **2018**, *18* (3), 1972−1977.

(11) Pan, C. F.; Shi, A.; Zhang, X. Y.; et al. Two-dimensional electron gas on the surface of alkali-earth metal based electrides: Assistance to overcome tunneling barriers in ohmic contacts. *Phys. Rev. B* **2024**, *110* (8), 085406.

(12) Wan, B.; Yuan, Y.; Zheng, L.; et al. BaCu, a Two-Dimensional Electride with Cu Anions. *J. Am. Chem. Soc.* **2024**, *146* (25), 17508−17516.

(13) Ming, W.; Yoon, M.; Du, M. H.; et al. First-Principles Prediction of Thermodynamically Stable Two-Dimensional Electrides. *J. Am. Chem. Soc.* **2016**, *138* (47), 15336−15344.

(14) McRae, L. M.; Radomsky, R. C.; Pawlik, J. T.; et al. Sc_2C, a 2D Semiconducting Electride. *J. Am. Chem. Soc.* **2022**, *144* (24), 10862−10869.

(15) Zhao, S.; Li, Z.; Yang, J. Obtaining two-dimensional electron gas in free space without resorting to electron doping: an electride based design. *J. Am. Chem. Soc.* **2014**, *136* (38), 13313−13318.

(16) Li, K.; Gong, Y.; Wang, J.; et al. Electron-Deficient-Type Electride Ca_5Pb_3: Extension of Electride Chemical Space. *J. Am. Chem. Soc.* **2021**, *143* (23), 8821−8828.

(17) Toda, Y.; Yanagi, H.; Ikenaga, E.; et al. Work Function of a Room-Temperature, Stable Electride $[Ca_{24}Al_{28}O_{64}]^{4+}(e^-)_4$. *Adv. Mater.* **2007**, *19* (21), 3564−3569.

(18) Dhakal, K. P.; Ghimire, G.; Chung, K.; et al. Probing Multiphased Transition in Bulk MoS2 by Direct Electron Injection. *ACS Nano* **2019**, *13* (12), 14437−14446.

(19) Wang, X. T.; Tang, W.; Cao, B.-H.; et al. Discovery and Prediction on a Family of Hard Superconductors with Kagome Lattice: XY_3 Compounds. *ACS Nano* **2025**, *19* (18), 17323−17335.

(20) Zhu, S.-C.; Wang, L.; Qu, J.-Y.; et al. Computational design of flexible electrides with nontrivial band topology. *Phys. Rev. Mater.* **2019**, *3* (2), 024205.

(21) Hirayama, M.; Matsuishi, S.; Hosono, H.; et al. Electrides as a New Platform of Topological Materials. *Phys. Rev. X* **2018**, *8* (3), 031067.

(22) Meng, W. Z.; Zhang, X. M.; Jiang, J. Y.; Li, Z.; Liu, Y.; Dai, X.; Liu, G. Multi-Dimensional Topological Fermions in Electrides. *Adv. Phys. Res.* **2023**, *2* (7), 2200119−2202604.

(23) Lim, C. Y.; Kim, M. S.; Lim, D. C.; Kim, S.; Lee, Y.; Cha, J.; Lee, G.; Song, S. Y.; Thapa, D.; Denlinger, J. D.; et al. Topological Fermi-arc surface state covered by floating electrons on a two-dimensional electride. *Nat. Commun.* **2024**, *15* (1), 5615.

(24) Zhang, Z.; You, J.-Y. Tunable Topological Phases in Two-Dimensional Electrides. *ACS Mater. Lett.* **2023**, *5* (7), 1870−1875.

(25) Zhou, J.; Song, X.; Yang, M.; et al. A first principles study of uniaxial strain-stabilized long−range ferromagnetic ordering in electrenes. *J. Mater. Chem. C* **2021**, *9* (46), 16576−16580.
(26) Kim, S. W.; Toda, Y.; Hayashi, K.; et al. Synthesis of a Room Temperature Stable $12CaO{\cdot}7Al_2O_3$ Electride from the Melt and Its Application as an Electron Field Emitter. *Chem. Mater.* **2006**, *18* (7), 1938−1944.
(27) Yanagi, H.; Kim, K.-B.; Koizumi, I.; et al. Low Threshold Voltage and Carrier Injection Properties of Inverted Organic Light-Emitting Diodes with $[Ca_{24}Al_{28}O_{64}]^{4+}(4e^-)$ Cathode and $Cu_{2-x}Se$ Anode. *J. Phys. Chem. C* **2009**, *113* (42), 18379−18384.
(28) Toda, Y.; Matsuishi, S.; Hayashi, K.; et al. Field Emission of Electron Anions Clathrated in Subnanometer-Sized Cages in $[Ca_{24}Al_{28}O_{64}]^{4+}(4e^-)$. *Adv. Mater.* **2004**, *16* (8), 685−689.
(29) Toda, Y.; Ishiyama, S.; Khutoryan, E.; et al. Rattling of Oxygen Ions in a Sub-Nanometer-Sized Cage Converts Terahertz Radiation to Visible Light. *ACS Nano* **2017**, *11* (12), 12358−12364.
(30) Meng, W. Z.; Wang, J. H.; Wang, X. T.; et al. Multi-dimensional inorganic electrides for energy conversion and storage. *J. Mater. Chem. A* **2024**, *12* (5), 2583−2604.
(31) Gong, Y. T.; Li, H. C.; Wu, J. Z.; et al. Unique Catalytic Mechanism for Ru-Loaded Ternary Intermetallic Electrides for Ammonia Synthesis. *J. Am. Chem. Soc.* **2022**, *144* (19), 8683−8692.
(32) Lu, Y. F.; Li, J.; Tada, T.; et al. Water Durable Electride Y_5Si_3: Electronic Structure and Catalytic Activity for Ammonia Synthesis. *J. Am. Chem. Soc.* **2016**, *138* (12), 3970−3973.
(33) Han, S. S.; Thacharon, A.; Kim, J.; Chung, K.; Liu, X.; Jang, W.; Jetybayeva, A.; Hong, S.; Lee, K. H.; Kim, Y.; et al. Boosted Heterogeneous Catalysis by Surface-Accumulated Excess Electrons of Non-Oxidized Bare Copper Nanoparticles on Electride Support. *Advanced Science* **2023**, *10* (2), No. e2204248.
(34) Kitano, M.; Inoue, Y.; Ishikawa, H.; et al. Essential role of hydride ion in ruthenium-based ammonia synthesis catalysts. *Chem. Sci.* **2016**, *7* (7), 4036−4043.
(35) Ye, T. N.; Lu, Y.; Li, J.; et al. Copper-Based Intermetallic Electride Catalyst for Chemoselective Hydrogenation Reactions. *J. Am. Chem. Soc.* **2017**, *139* (47), 17089−17097.
(36) Wu, J.; Li, J.; Gong, Y.; et al. Intermetallic Electride Catalyst as a Platform for Ammonia Synthesis. *Angew. Chem., Int. Ed.* **2019**, *58* (3), 825−829.
(37) Kammert, J.; Moon, J.; Cheng, Y.; et al. Nature of Reactive Hydrogen for Ammonia Synthesis over a $Ru/C_{12}A_7$ Electride Catalyst. *J. Am. Chem. Soc.* **2020**, *142* (16), 7655−7667.
(38) Gong, Y. T.; Li, H. C.; Li, C.; et al. LaRuSi Electride Disrupts the Scaling Relations for Ammonia Synthesis. *Chem. Mater.* **2022**, *34* (4), 1677−1685.
(39) Cao, Y.; Liu, P. T.; Li, J. X.; et al. Microscopic Mechanism of Enhanced Catalytic Activity for Ammonia Synthesis in Y_5M_3(M = Si/Ge) Electrides. *J. Phys. Chem. C* **2023**, *127* (6), 2953−2962.
(40) Yu, X. B.; Moon, J. S.; Cheng, Y. Q.; et al. In Situ Neutron Scattering Study of the Structure Dynamics of the $Ru/Ca_2N{:}e^-$ Catalyst in Ammonia Synthesis. *Chem. Mater.* **2023**, *35* (6), 2456−2462.
(41) Zhang, X. Y.; Li, Z. C.; Xu, M.; et al. Recent progress and prospects in active anion-bearing $C_{12}A_7^-$mediated chemical reactions. *J. Mater. Chem. A* **2023**, *11* (28), 15074−15099.
(42) Kitano, M.; Inoue, Y.; Yamazaki, Y.; et al. Ammonia synthesis using a stable electride as an electron donor and reversible hydrogen store. *Nat. Chem.* **2012**, *4* (11), 934−940.
(43) Sharif, M. J.; Kitano, M.; Inoue, Y.; et al. Electron Donation Enhanced CO Oxidation over Ru-Loaded $12CaO{\cdot}7Al_2O_3$ Electride Catalyst. *J. Phys. Chem. C* **2015**, *119* (21), 11725−11731.
(44) Guo, J.; Chang, F.; Wang, P.; et al. Highly Active $MnN{-}Li_2NH$ Composite Catalyst for Producing CO_x-Free Hydrogen. *ACS Catal.* **2015**, *5* (5), 2708−2713.
(45) Yang, J.; Pan, J.; Deng, J.; et al. Vacancy-Induced Anionic Electrons in Single-Metal Oxides and Their Possible Applications in Ammonia Synthesis. *J. Am. Chem. Soc.* **2024**, *146* (30), 21160−21167.
(46) Chang, F.; Tezsevin, I.; de Rijk, J. W.; et al. Potassium hydride-intercalated graphite as an efficient heterogeneous catalyst for ammonia synthesis. *Nat. Catal.* **2022**, *5*, 222−230.
(47) Hosono, H. Spiers Memorial Lecture: Catalytic activation of molecular nitrogen for green ammonia synthesis: introduction and current status. *Faraday Discuss.* **2023**, *243*, 9−26.
(48) Zhang, Z. J.; Jiang, Y. H.; Li, J.; et al. A 2D Ba_2N Electride for Transition Metal-Free N_2 Dissociation under Mild Conditions. *J. Am. Chem. Soc.* **2023**, *145* (45), 24482−24485.
(49) Zhang, X.; Meng, W.; Liu, Y.; et al. Magnetic Electrides: High-Throughput Material Screening, Intriguing Properties, and Applications. *J. Am. Chem. Soc.* **2023**, *145* (9), 5523−5535.
(50) Mizoguchi, H.; Park, S.-W.; Katase, T.; et al. Origin of Metallic Nature of Na_3N. *J. Am. Chem. Soc.* **2021**, *143* (1), 69−72.
(51) Savin, A.; Nesper, R.; Wengert, S.; et al. ELF: The Electron Localization Function. *Angew Chem. Int. Ed. Engl.* **1997**, *36* (17), 1808−1832.
(52) Zhang, Y.; Wang, H.; Wang, Y.; et al. Computer-Assisted Inverse Design of Inorganic Electrides. *Phys. Rev. X* **2017**, *7* (1), 011017.
(53) Dale, S. G.; Johnson, E. R. Theoretical Descriptors of Electrides. *J. Phys. Chem. A* **2018**, *122* (49), 9371−9391.
(54) Yang, R.; Mei, L.; Lin, Z.; et al. Intercalation in 2D materials and in situ studies. *Nat. Rev. Chem.* **2024**, *8*, 410−432.
(55) He, X.; Wang, H.; Sun, J.; et al. Intercalation of functional materials with phase transitions for neuromorphic applications. *Matter* **2025**, *8* (1), 101893.
(56) Zhao, J.; Li, L.; Li, P.; et al. Realization of 2D metals at the ångström thickness limit. *Nature* **2025**, *639*, 354−359.
(57) You, J.-Y.; Gu, B.; Su, G.; et al. Emergent Kagome Electrides. *J. Am. Chem. Soc.* **2022**, *144* (12), 5527−5534.
(58) Zhang, Y.-F.; Pan, J.; Banjade, H.; et al. Two-dimensional MX Dirac materials and quantum spin Hall insulators with tunable electronic and topological properties. *Nano Res.* **2021**, *14* (3), 584−589.
(59) Zhou, J.; Feng, Y. P.; Shen, L. Atomic-orbital-free intrinsic ferromagnetism in electrenes. *Phys. Rev. B* **2020**, *102* (18), 180407.
(60) Kresse, G.; Furthmuller, J. Efficiency of ab-initio total energy calculations for metals and semiconductors using a plane-wave basis set. *Comput. Mater. Sci.* **1996**, *6* (1), 15−50.
(61) Kresse, G.; Furthmuller, J. Efficient iterative schemes for ab initio total-energy calculations using a plane-wave basis set. *Phys. Rev. B* **1996**, *54* (16), 11169−11186.
(62) Blochl, P. E. Projector augmented-wave method. *Phys. Rev. B* **1994**, *50* (24), 17953−17979.
(63) Perdew, J. P.; Burke, K.; Ernzerhof, M. Generalized Gradient Approximation Made Simple. *Phys. Rev. Lett.* **1996**, *77*, 3865−3868.
(64) Heyd, J.; Scuseria, G. E.; Ernzerhof, M. Hybrid functionals based on a screened Coulomb potential. *J. Chem. Phys.* **2003**, *118* (18), 8207−8215.
(65) Monkhorst, H. J.; Pack, J. D. Special points for Brillouin-zone integrations. *Phys. Rev. B* **1976**, *13* (12), 5188−5192.
(66) Grimme, S.; Antony, J.; Ehrlich, S.; Krieg, H. A consistent and accurateab initioparametrization of density functional dispersion correction (DFT-D) for the 94 elements H-Pu. *J. Chem. Phys.* **2010**, *132* (15), 154104.
(67) Togo, A.; Tanaka, I. First principles phonon calculations in materials science. *Scr. Mater.* **2015**, *108*, 1−5.
(68) Mostofi, A. A.; Yates, J. R.; Lee, Y.-S.; et al. Wannier90: A tool for obtaining maximally-localised Wannier functions. *Comput. Phys. Commun.* **2008**, *178* (9), 685−699.
(69) Marzari, N.; Mostofi, A. A.; Yates, J. R.; et al. Maximally localized Wannier functions: Theory and applications. *Rev. Mod. Phys.* **2012**, *84* (4), 1419−1475.
(70) Wu, Q.; Zhang, S.; Song, H.-F.; et al. WannierTools: An open-source software package for novel topological materials. *Comput. Phys. Commun.* **2018**, *224*, 405−416.

https://doi.org/10.1021/acsnano.5c13653
ACS Nano 2025, 19, 39915−39924

(71) Henkelman, G.; Uberuaga, B. P.; Jónsson, H. A climbing image nudged elastic band method for finding saddle points and minimum energy paths. *J. Chem. Phys.* **2000**, *113* (22), 9901−9904.
(72) Sheppard, D.; Xiao, P.; Chemelewski, W.; Johnson, D. D.; Henkelman, G. A generalized solid-state nudged elastic band method. *J. Chem. Phys.* **2012**, *136* (7), 074103.
(73) Sheppard, D.; Terrell, R.; Henkelman, G. Optimization methods for finding minimum energy paths. *J. Chem. Phys.* **2008**, *128* (13), 134106.
(74) Sheppard, D.; Henkelman, G. Paths to which the nudged elastic band converges. *J. Comput. Chem.* **2011**, *32* (8), 1769−1771.

https://doi.org/10.1021/acsnano.5c13653
ACS Nano 2025, 19, 39915−39924